

1 **Trajectory model simulations of ozone (O<sub>3</sub>) and carbon monoxide (CO) transport in**  
2 **the lower stratosphere (LS)**

3  
4 T. Wang<sup>1</sup>, W. J. Randel<sup>2</sup>, A. E. Dessler<sup>1</sup>, M. R. Schoeberl<sup>3</sup>, D. E. Kinnison<sup>2</sup>

- 5  
6 1. Texas A&M University, College Station, TX, USA  
7 2. National Center for Atmospheric Research (NCAR), Boulder, CO, USA  
8 3. Science and Technology Corporation, Lanham, MD, USA  
9

10 *\*Correspondence to:* Tao Wang (tao.wang@tamu.edu)

11  
12 **Abstract**

13  
14 A domain-filling, forward trajectory model originally developed for simulating  
15 stratospheric water vapor is used to simulate ozone (O<sub>3</sub>) and carbon monoxide (CO) in  
16 the lower stratosphere (LS). Trajectories are initialized in the upper troposphere, and the  
17 circulation is based on reanalysis wind fields. In addition, chemical production and loss  
18 rates along trajectories are included using calculations from the Whole Atmosphere  
19 Community Climate Model (WACCM). The trajectory model results show good overall  
20 agreement with satellite observations from the Aura Microwave Limb Sounder (MLS)  
21 and the Atmospheric Chemistry Experiment Fourier Transform Spectrometer (ACE-FTS)  
22 in terms of spatial structure and seasonal variability. The trajectory model results also  
23 agree well with the Eulerian WACCM simulations. Analysis of the simulated tracers  
24 shows that seasonal variations in tropical upwelling exerts strong influence on O<sub>3</sub> and CO  
25 in the tropical lower stratosphere, and the coupled seasonal cycles provide a useful test of  
26 the transport simulations. Interannual variations in the tracers are also closely coupled to  
27 changes in upwelling, and the trajectory model can accurately capture and explain  
28 observed changes during 2005-2011. This demonstrates the importance of variability in  
29 tropical upwelling in forcing chemical changes in the tropical lower stratosphere.  
30

31 **1. Introduction**

32 The influx of water vapor (H<sub>2</sub>O) to the stratosphere is largely determined by the large-  
33 scale troposphere-to-stratosphere transport in the tropics, during which air is dehydrated  
34 across the cold tropical tropopause (e.g., Fueglistaler et al., 2009 and references therein).  
35 Observations such as the entry mixing ratios (Dessler, 1998; Dessler et al., 2013), the

36 coherent relations between water vapor and temperature (Mote et al., 1996), and the  
37 extensive cirrus clouds near the tropopause (e.g., Winker and Trepte, 1998; Wang and  
38 Dessler, 2012) all support this understanding. Back trajectory models have provided  
39 detailed simulations of stratospheric H<sub>2</sub>O (e.g. Fueglistaler et al., 2005). More recently, a  
40 newly designed domain-filling forward trajectory model driven by reanalysis wind and  
41 temperature has demonstrated success at simulating the transport of H<sub>2</sub>O in the  
42 stratosphere (Schoeberl and Dessler, 2011; Schoeberl et al., 2012; Schoeberl et al., 2013).  
43 In this trajectory model, winds determine the pathways of parcels and temperature  
44 determines the H<sub>2</sub>O content through an idealized saturation calculation. This simple  
45 advection-condensation strategy yields reasonable results for H<sub>2</sub>O in the stratosphere,  
46 although the detailed results depend on the wind and temperature fields utilized and  
47 assumptions regarding supersaturation (*Liu et al.*, 2010; Schoeberl et al., 2012).

48 Besides H<sub>2</sub>O, ozone (O<sub>3</sub>) and carbon monoxide (CO) are also important trace  
49 gases in the stratosphere linked to circulation, transport and climate forcing (for O<sub>3</sub>).  
50 Ozone abundances in the stratosphere cover a wide dynamic range (~10's of ppbv to a  
51 few ppmv), and are influenced by a variety of chemical and dynamical processes,  
52 including photochemical production and loss and large- and small-scale transport (for  
53 example, deep convective lofting of boundary layer low O<sub>3</sub> air to the upper troposphere,  
54 e.g. Folkins et al., 2002). CO behaves as a tropospheric source gas, originating from  
55 natural and anthropogenic emissions, including combustion processes near the surface  
56 and oxidation of methane and other hydrocarbons within the troposphere. The main sink  
57 of CO is oxidation by the hydroxyl radical (OH) (Logan et al., 1981). The CO  
58 photochemical lifetime of 2-3 months makes it a useful tracer for transport studies in the  
59 troposphere and lower stratosphere (e.g., Bowman, 2006; Schoeberl et al., 2006, 2008).

60 The purpose of this work is to simulate O<sub>3</sub> and CO in the lower stratosphere (LS)  
61 using the domain-filling, forward trajectory model used previously for stratospheric H<sub>2</sub>O.  
62 Trajectory modeling of O<sub>3</sub> and CO can provide useful tests for simplified understanding  
63 of transport and chemical processes in the stratosphere, and provide complementary  
64 information to the H<sub>2</sub>O simulations (which are primarily constrained by tropopause  
65 temperatures). In addition to testing circulation and transport within the trajectory model,  
66 the O<sub>3</sub> and CO simulations can provide understanding of mechanisms leading to observed

67 chemical behavior, including transport history and pathways, seasonal and interannual  
68 variations, and relation to the stratospheric age-of-air (Waugh and Hall, 2002). Ozone  
69 and CO are complementary tracers representing primarily stratospheric and tropospheric  
70 sources; both tracers exhibit strong gradients across the tropopause, and they are often  
71 combined using tracer correlations to understand transport and chemical behavior in the  
72 upper troposphere and lower stratosphere (UTLS) (e.g., Fischer et al., 2000). Furthermore,  
73 O<sub>3</sub> and CO exhibit relatively large out-of-phase seasonal cycles in the tropical lower  
74 stratosphere (Randel et al., 2007), and these coupled variations provide a sensitive test of  
75 the trajectory model simulations in this region.

76

## 77 **2. Model Description and Data Used**

78

### 79 **2.1 Trajectory Model**

80

81 The trajectory model used here follows the details described in Schoeberl and Dessler  
82 (2011) and Schoeberl et al. (2012), with trajectories calculated using the Bowman  
83 trajectory code (Bowman, 1993; Bowman and Carrie, 2002; Bowman et al., 2013).  
84 Because of the overly dispersive behavior of kinematic trajectories (e.g., Schoeberl et al.,  
85 2003; Liu et al., 2010; Ploeger et al., 2010; Schoeberl and Dessler, 2011), we perform  
86 diabatic trajectories using isentropic coordinates, in which the vertical velocity is the  
87 potential temperature tendency converted from the diabatic heating rates via the  
88 thermodynamic equation (Andrews et al., 1987).

89 The methodology for the trajectory simulations of O<sub>3</sub> and CO follows Schoeberl  
90 and Dessler (2011) and Schoeberl et al. (2012), wherein the parcels are initialized at the  
91 370-K isentrope, below the tropical tropopause, using climatological O<sub>3</sub> and CO from the  
92 MLS (monthly means averaged over 2005-2011) to provide approximate entry level  
93 values in the upper troposphere. The 370 K level is chosen as the initialization level  
94 because it is above the level of zero net heating rates and parcels there tend to ascend to  
95 the stratosphere (see Discussion). To account for chemical changes along the trajectories,  
96 we use chemical production and loss rates output from WACCM. Specifically, the O<sub>3</sub> and

97 CO concentration carried by each parcel is modified from the previous time step using  
98 the production and loss frequencies calculated from WACCM.

99 For each day 1350 parcels are initiated on an equal area grid covering 40° N-S  
100 latitude and advected forward in time by reanalysis winds. At the end of each day, any  
101 parcels that have descended below the 250-hPa level are removed since in most cases  
102 they have re-entered the troposphere. The upper boundary is chosen to be the ~2200-K  
103 isentrope (~1 hPa or ~50 km) to cover the entire stratosphere. Parcels are initialized and  
104 added to the ensemble consecutively each day and the combined set of parcels is then run  
105 forward. This process is repeated over the entire integration period. As more and more  
106 parcels are injected into the model, the stratospheric domain is filled up with parcels –  
107 this is the concept of domain-filling used in our model. The trajectory model simulations  
108 are started in January 1990 and integrated to the end of 2011; after 3-4 years the system  
109 reaches steady state with approximately 1 million parcels in the domain. We focus on  
110 analyzing the model results during 2005-2011, to overlap the MLS and ACE-FTS  
111 observations.

112 Upwelling across the tropical tropopause in the trajectory model is determined by  
113 the reanalysis total diabatic heating rates ( $Q_{\text{tot}}$ , hereinafter  $Q$ ), which include heating due  
114 to long-wave and short-wave radiation, moist physics, friction, gravity wave drags, etc.  
115 As shown below, our simulations of  $O_3$  and CO are sensitive to the imposed upwelling.  
116 There is substantial uncertainty in the detailed magnitude and spatial structure of  $Q$ , as  
117 seen in the differences among separate reanalysis results (Schoeberl et al. 2012; Randel  
118 and Jensen, 2013; Wright and Fueglistaler, 2013). Figure 1 illustrates the differences in  
119  $Q$  in the tropics (15° N-S) based on several reanalysis data sets, highlighting large  
120 differences in the UTLS. Given this uncertainty, we tested the sensitivity of our  
121 calculations to variations in the heating rates by comparing results based on the NASA  
122 Modern Era Retrospective-Analysis for Research and Applications (MERRA, Rienecker  
123 et al., 2011) and the ECMWF ERA Interim reanalysis (ERAi, Dee et al., 2011). Below  
124 we highlight the sensitivity of the resulting  $O_3$  and CO simulations to these imposed  
125 circulations.

126 Changes in chemical concentrations in the trajectory model are calculated using  
127 the chemical continuity equation (e.g., *Dessler*, 2000):

128 
$$[\chi]_{current} = [\chi]_{previous} + (P_{\chi} - LF_{\chi} \cdot [\chi]_{previous}) \cdot \Delta t \quad (1)$$

129 Here,  $\chi$  represents either O<sub>3</sub> or CO. Current chemical concentrations  $[\chi]_{current}$  in volume  
130 mixing ratio (VMR) are determined by concentrations in previous time step  $[\chi]_{previous}$   
131 and the net change, derived from the production minus loss occurring in each time step.  
132 The production rate  $P_{\chi}$  in VMR per unit time is obtained from WACCM. The loss rate  
133 ( $LF_{\chi} \cdot [\chi]_{previous}$ ) in VMR per unit time is calculated as a product of loss frequency  $LF_{\chi}$   
134 (per unit time) times the chemical concentration (VMR), representing a linear chemical  
135 loss. The loss frequencies are estimated from WACCM by dividing the model loss  
136 rate  $L_{\chi}$  by the chemical concentration  $[\chi]$ , i.e.,  $LF_{\chi} = L_{\chi}/[\chi]$ . In our simulation  $P_{\chi}$  and  
137  $LF_{\chi}$  are calculated from WACCM as a function of latitude, altitude, and climatological  
138 months. The time step for calculating trajectories is 45-min while the time step for  
139 calculating chemical changes is 1-day.

140

## 141 **2.2 WACCM Chemical Production and Loss Rates**

142

143 The chemical production and loss rates from the Whole Atmosphere Community Climate  
144 Model (WACCM4) (Garcia et al., 2007) are applied in our model to represent chemical  
145 processes. The vertical domain of WACCM4 extends from the surface to the lower  
146 thermosphere, with horizontal resolution of  $2.5^{\circ} \times 1.9^{\circ}$  in longitude and latitude and 88  
147 levels up to ~150 km. In the UTLS the vertical resolution is 1.1–1.4 km. The WACCM4  
148 simulation used here is run with specified dynamics (SD) fields (Lamarque et al., 2012),  
149 in which the model is nudged by the MERRA meteorological fields (Rienecker et al.,  
150 2011) from January 2004 to December 2011 (hereafter we only use WACCM to  
151 represent SD-WACCM4).

152 Figure 2 shows the annual zonal mean ratio of net tendency (production rate  
153 minus loss rate) divided by the loss rate for O<sub>x</sub> and CO. These show the mean differences  
154 of production to loss, with positive numbers indicating net chemical increase and  
155 negative numbers indicating net chemical decrease; values close to zero imply balanced  
156 production vs. loss. On the background are the respective photochemical lifetimes  
157 evaluated from the loss rates ( $\tau_L = [\chi]/L_{\chi}$ ). Both O<sub>x</sub> and CO exhibit relatively long

158 lifetimes ( $> 3$  months) in the lower-middle stratosphere, and hence transport will have a  
159 dominant influence on their distributions. Above  $\sim 30$  km the lifetimes are shorter, and  
160 the photochemical behavior will determine chemical structure.

161 Here  $O_x$  is the odd oxygen – the sum of  $O_3$  and  $O$ . We use the production and loss  
162 rates of  $O_x$  because (1) the time step of trajectory model is 1 day, which is much longer  
163 than the lifetime of  $O_3$  in the middle and upper stratosphere, and (2) the abundances of  $O_3$   
164 only change on time scales comparable to or longer than the lifetime of  $O_x$  (see e.g.  
165 Dessler, 2000, chapter 3). Therefore, it is reasonable to use production and loss rate of  $O_x$   
166 instead of  $O_3$  for our purpose of simulation. Because  $O_3$  abundance is much greater than  
167  $O$ , i.e.,  $O_x \approx O_3$ , throughout the rest of the paper we use  $O_3$  and  $O_x$  interchangeably.

168  $O_x$  production in the stratosphere is almost entirely due to the photolysis of  $O_2$ .  
169  $P_{O_x}$  increases with altitude over most of the stratosphere because the photolysis rate  
170 (proportional to solar radiation) increases faster with altitude than  $[O_2]$  decreases, so the  
171 net effect is increasing. Figure 2a shows that from 150 to  $\sim 10$  hPa  $O_x$  production exceeds  
172 loss in the tropics, whereas a net chemical decrease of  $O_3$  occurs in mid- to high latitudes  
173 (transport of  $O_3$  from the tropics to higher latitudes closes the budget). Between about 10  
174 and 2 hPa the daily production and loss of  $O_x$  become comparable and the system is in  
175 diurnal steady state. The system gradually reaches photochemical steady states above  $\sim 2$   
176 hPa, where the lifetime of  $O_x$  is less than a day and the instantaneous production and loss  
177 can be treated equal throughout the day. Here we simply set the  $[O_x]$  to be  $(P_{O_x}/LF_{O_x})$  in  
178 our trajectory calculations.

179 In the UTLS region, the main source of CO is from the troposphere (from direct  
180 emissions and photochemical production), and this source is accounted for by initializing  
181 trajectories with observed values of CO. There is a net chemical decrease (Fig. 2b) in the  
182 UTLS, where CO is predominantly removed by oxidation with OH. CO experiences a net  
183 increase in the middle stratosphere (above  $\sim 24$  km) due to oxidation of methane ( $CH_4$ ),  
184 although this has little influence on the results shown here.

185 In our simulation  $P_x$  and  $LF_x$  are calculated from WACCM as a function of  
186 latitude, altitude, and climatological months averaged over 2005-2011, so that a constant  
187 annual cycle is applied throughout the model integration. As discussed in Sect. 5, this

188 calculation will not accurately handle the situation where chemical losses are linked to  
189 meteorological behavior, such as for ozone losses in the polar winter stratosphere.

190

### 191 **2.3 MLS Observations of O<sub>3</sub> and CO**

192

193 We will compare the model to observations of O<sub>3</sub> and CO from the Aura Microwave  
194 Limb Sounder (MLS) (Waters et al., 2006). MLS climatology (constant annual cycle) of  
195 O<sub>3</sub> and CO averaged from August 2004 to December 2012 is used to set the initial  
196 abundances when parcels are initialized at the 370 K level, and the observations at higher  
197 levels are used to evaluate the trajectory model results. We use the MLS version 3.3  
198 (v3.3) Level 2 products, described in the data quality and description document  
199 ([http://mls.jpl.nasa.gov/data/v3-3\\_data\\_quality\\_document.pdf](http://mls.jpl.nasa.gov/data/v3-3_data_quality_document.pdf)). O<sub>3</sub> profiles are available  
200 at 12 levels per decade from 261 to 0.02 hPa and CO profiles are available between 215  
201 and 0.0046 hPa at 6 levels per decade. The vertical resolution of O<sub>3</sub> in the UTLS is  
202 approximately 2.5-3 km while for CO it is ~ 4.5-5 km. The detailed validation for these  
203 data sets can be found in Froidevaux et al., (2008), Pumphrey et al., (2007), and Livesey  
204 et al., (2008).

205 For the comparisons shown here, we applied the MLS O<sub>3</sub> and CO averaging  
206 kernels to both our trajectory simulations and WACCM model outputs when comparing  
207 with the MLS observations. We have followed the detailed instructions for applying  
208 averaging kernels as described in [http://mls.jpl.nasa.gov/data/v3-](http://mls.jpl.nasa.gov/data/v3-3_data_quality_document.pdf)  
209 [3\\_data\\_quality\\_document.pdf](http://mls.jpl.nasa.gov/data/v3-3_data_quality_document.pdf).

210

### 211 **2.4 Other Verifying Datasets**

212

213 Besides using chemical production and loss from the WACCM, we also compare O<sub>3</sub> and  
214 CO modeled by WACCM to the trajectory model simulations, which serves as a sanity  
215 check of applying the imposed WACCM chemistry, and also as a simple comparison of  
216 Lagrangian vs. Eulerian model results. We also compare the trajectory modeling to the  
217 CO measurements from the Atmospheric Chemistry Experiment Fourier Transform  
218 Spectrometer (ACE-FTS) (Bernath et al., 2005), which shows some systematic

219 differences from MLS retrievals in the stratosphere (Clerbaux et al., 2008; Park et al.,  
220 2013). A detailed description of the ACE CO observations can be found in Park et al.,  
221 (2013).

222

### 223 **3. Trajectory Modeling Results**

#### 224 **3.1 O<sub>3</sub> Results**

225

226 Figure 3 shows the zonal mean cross section of O<sub>3</sub> during December-February (DJF)  
227 from the trajectory model driven by ERAi reanalysis (denoted as “TRAJ\_ERAi”),  
228 compared to both the MLS observations and the WACCM results. Because O<sub>3</sub> above 10  
229 hPa is in photochemical steady-state (Sect. 2) we focus on O<sub>3</sub> below 10 hPa. Overall the  
230 trajectory simulations agree with results from both MLS and WACCM. In the lower  
231 stratosphere transport plays an important role in re-distributing chemical species,  
232 resulting in contours of O<sub>3</sub> approximately following the isentropes. The enhanced O<sub>3</sub>  
233 production due to photolysis at 30 km (~10 hPa) shifts from south during DJF towards  
234 north during JJA (not shown), following the seasonal variations of photolysis rates.

235 Vertical profiles of O<sub>3</sub> averaged over the deep tropics (18° N-S) from 2005 to  
236 2011 are shown in Fig. 4a (note that the x-axis is in log scale). The trajectory model  
237 driven by MERRA (denoted as “TRAJ\_MER”) shows reasonable agreement with MLS  
238 data (and WACCM) in the lower stratosphere, while the results based on ERAi (denoted  
239 as “TRAJ\_ERAi”) show relatively smaller O<sub>3</sub> values. Above 24 km where photochemical  
240 processes dominate, different trajectory runs yield similar results and they both agree  
241 with MLS and WACCM data. Note that the MERRA and ERAi simulations use identical  
242 O<sub>3</sub> initial values at 370 K, so that the differences in Fig. 4a are primarily a result of  
243 differences in upward circulation (Fig. 1). The mean differences in ozone in the lower  
244 stratosphere can be explained as a result of the different heating rates (vertical  
245 circulations) imposed. The ERAi heating rates are higher than MERRA up to 20 km (Fig.  
246 1). Due to positive vertical gradient in O<sub>3</sub> the stronger circulation moves air with lower  
247 O<sub>3</sub> upward, creating a lower relative concentration compared to MERRA.

248 Monthly time series of O<sub>3</sub> at 100 hPa and 68 hPa averaged over the deep tropics  
249 (18° N-S) are shown in Fig. 4b. There is a strong annual cycle in ozone at these levels

250 related to the seasonal variations in tropical upwelling (Randel et al., 2007; Abalos et al.,  
251 2012, 2013a), and this behavior is reproduced by the trajectory model, showing  
252 reasonable agreement in amplitude with the MLS observations and WACCM results (in  
253 spite of the differences in mean values). There are somewhat larger differences in annual  
254 cycle amplitude at 68 hPa, with the ERAi trajectory results showing better agreement  
255 with MLS.

256 The simulated and observed latitudinal structure of zonal mean O<sub>3</sub> in the lower  
257 stratosphere (68 hPa) throughout the seasonal cycle is shown in Fig. 5. The overall  
258 variations are reasonably well simulated by the trajectory model, although low biases are  
259 found compared to MLS over middle-to-high latitudes in both hemispheres (and  
260 WACCM is systematically higher over the globe). The development of the Antarctic  
261 ozone hole is evident in the very low ozone values polewards of 60° S in October, which  
262 is simulated in the trajectory model based on the strong chemical ozone losses in this  
263 region derived from WACCM.

264 Figure 6 compares the horizontal structure of boreal summer (JJA) O<sub>3</sub> at 83 hPa  
265 from MLS data and the trajectory results driven by MERRA. The trajectory results show  
266 a reasonable simulation of the spatial patterns compared to MLS (and WACCM; not  
267 shown), with a clear minimum inside the Asian monsoon anticyclone linked to upward  
268 transport of ozone-poor air from lower levels (Park et al., 2009). There is also relatively  
269 low O<sub>3</sub> centered near 15° S linked to the slow ascending air from the troposphere in this  
270 region.

271 The trajectory model is also able to capture the spatial behavior of polar ozone.  
272 Figure 7 shows a comparison of high latitude O<sub>3</sub> in the Northern Hemisphere (NH) during  
273 winter (DJF) and in the Southern Hemisphere (SH) during spring (September) between  
274 MLS and trajectory modeling driven by both MERRA and ERAi winds. During NH  
275 winter, O<sub>3</sub> rich air (> 2.2 ppmv) occurs within the polar vortex (denoted with the 24 PVU  
276 isopleth in Fig. 7a-c), and the trajectory model captures the observed isolation from  
277 middle latitudes, although differences in magnitude exist. During SH springtime, the  
278 Antarctic ozone hole (denoted with the 195 K isotherm in Fig. 7d-f) is reasonably well  
279 reproduced in the trajectory model based on imposed WACCM chemistry. The trajectory  
280 model also captures the spatial structure of the zonal wave ozone maximum near 50° S

281 (the so-called “ozone croissant”), linked to the descending branch of the BD circulation.  
282 The weaker extra-vortex high in ozone in the trajectory model may be related to the  
283 weaker overall circulation in MERRA compared to observations (Schoeberl et al., 2012,  
284 2013). Noted that due to the climatological loss frequency adopted from WACCM, this  
285 model cannot account for interactions of circulation and chemistry, which affects O<sub>3</sub>  
286 mostly in winter polar regions (see Discussion).

287

### 288 **3.2 CO Results**

289

290 Figure 8 shows that zonal mean cross sections of CO from ACE-FTS, WACCM, and the  
291 trajectory model agree well in the lower stratosphere. CO has a maximum in the tropical  
292 upper troposphere, and decreases with altitude due to OH oxidation to a minimum near  
293 22 km. CO increases above this altitude due to production from methane (CH<sub>4</sub>) oxidation.  
294 The ACE-FTS observations show high CO mixing ratios in the polar middle and upper  
295 stratosphere regions, resulting from the downward transport of CO from the mesosphere  
296 (from photodissociation of CO<sub>2</sub>); this behavior is also seen (to a weaker degree) in  
297 WACCM, but is not simulated in the trajectory model, which does not include  
298 mesospheric processes.

299 Figure 9a shows the CO vertical profiles and time series averaged in the deep  
300 tropics (15° N-S). Due to the differences of MLS and ACE-FTS retrievals in the  
301 stratosphere, here we also included ACE CO for comparison. The vertical profiles in Fig.  
302 9a show broad-scale agreements, although there are differences among the trajectory  
303 models (with ERAi driven results larger than those driven by MERRA) and also between  
304 the ACE-FTS and MLS observations (all of the models agree better with the ACE  
305 observations above 22 km). Time series of CO at 100 hPa (Fig. 9b) show a semi-annual  
306 cycle linked to initialized variations in the upper troposphere (Liu et al., 2007), with  
307 approximate agreement among the models and observations (with slightly larger values  
308 in the MLS data). The variability changes to an annual cycle at 68 hPa, as a response to  
309 variations in tropical upwelling. At 68 hPa the annual cycle is captured in a reasonable  
310 manner in the models, with the ERAi results showing better agreement with MLS and  
311 ACE-FTS data.

312 A further diagnostic to evaluate the model simulations is made by plotting  
313 monthly tropical (15° N-S) averages of O<sub>3</sub> vs. CO in the lower stratosphere (68 hPa), as  
314 shown in Fig. 10. This includes the observations from MLS, together with trajectory  
315 model simulations driven by both MERRA and ERAi, which shows the sensitivity to  
316 different Q (see also Fig. 1). There is an overall anti-correlation between O<sub>3</sub> and CO in  
317 Fig. 10, mainly representing the out-of-phase annual cycles seen in Figs. 4b and 9b. The  
318 comparisons in Fig. 10 show that stronger upwelling in the ERAi simulation produces  
319 slightly lower values of O<sub>3</sub> and higher values in CO (> 30 ppbv), in better agreement with  
320 MLS data. Moreover, the slope of the CO-O<sub>3</sub> variations in the ERAi simulation  
321 approximately matches the MLS result.

322 The DJF and JJA seasonal distributions of CO at 68 hPa from the ERAi trajectory  
323 model are compared to MLS data in Fig. 11. In both seasons the trajectory model shows  
324 spatial patterns consistent with MLS data. During DJF the patterns show a center of high  
325 CO over central America and enhancements over South East Asia, extending to the  
326 tropical western Pacific (largely attributable to fossil fuel emissions, Jiang et al., 2007).  
327 The trajectory model also captures the well-known CO maximum linked to the Asian  
328 monsoon anticyclone during JJA, which is substantially stronger at the 100-hPa level (e.g.,  
329 Randel and Park, 2006; Park et al., 2009; Randel et al., 2010).

330 Overall, the large-scale seasonal behavior of CO simulated by the trajectory  
331 model is in agreement with both observations (MLS and ACE-FTS) and Eulerian  
332 chemical model (WACCM), although the results are sensitive to the tropical upwelling  
333 speed (see Discussion).

334

#### 335 **4. Interannual Variability of Tracers in the Tropical Lower Stratosphere (LS)**

336 The coherent seasonal variations in O<sub>3</sub> and CO in the tropical LS demonstrate that  
337 transport processes have a large impact on the chemical concentrations in this region. The  
338 Eulerian-mean calculations of *Abalos et al.* (2012, 2013a) show that tropical upwelling is  
339 the main driver of the annual cycles in O<sub>3</sub> and CO above the tropical tropopause. Our  
340 Lagrangian trajectory model results (Figs. 4b and 9b) also show that the annual cycles of  
341 O<sub>3</sub> and CO above the tropopause (especially around 70 hPa) are strongly influenced by  
342 the tropical upwelling (Brewer-Dobson) circulation.

343 We further explore interannual variations in the chemical tracers and links to  
 344 changes in the upwelling circulation. Figure 12 shows the interannual anomalies (by  
 345 removing the annual cycle) in O<sub>3</sub> and CO concentrations in the tropical lower  
 346 stratosphere from MLS observations and from trajectory calculations, and in addition  
 347 anomalies in diabatic heating rates (upwelling) from reanalysis at 68 hPa. While there are  
 348 significant differences in time-mean diabatic heating rates between MERRA and ERAi  
 349 (Fig. 1), interannual changes in Q (Fig. 12c) show good agreement. Figure 12 shows that  
 350 interannual anomalies in O<sub>3</sub> and CO are strongly anti-correlated (due to oppositely signed  
 351 vertical gradient) and closely linked to interannual changes in diabatic heating.  
 352 Furthermore, Fig. 12 shows that trajectory calculations driven by both MERRA and  
 353 ERAi are able to simulate the observed interannual anomalies in O<sub>3</sub> and CO, in spite of  
 354 significant differences for the background seasonal cycle (Fig. 4b and 9b).

355 Taking results from the MERRA run as an example, the close relationship  
 356 between anomalies in diabatic heating and O<sub>3</sub> is quantified in Fig. 13a, which shows  
 357 strong anti-correlation with explained variance  $r^2=0.73$  and slope  $\Delta O_3/\Delta Q = -1.05 \pm 0.14$   
 358 (ppmv)/(K/day). Similar strong correlation is found for CO and Q anomalies (Fig. 13b),  
 359 with explained variance  $r^2=0.85$  and slope of  $31.11 \pm 2.86$  (ppbv)/(K day<sup>-1</sup>). The sign of  
 360 the slopes in Figs. 13a-b are opposite because of the different background vertical  
 361 gradients for O<sub>3</sub> and CO. These strong relationships between diabatic heating (Q) and  
 362 tracer anomalies highlight the dominant role of tropical upwelling in controlling species  
 363 with strong vertical gradients near the tropical tropopause.

364 Figure 12 also highlights strong anti-correlations between O<sub>3</sub> and CO anomalies,  
 365 which is further demonstrated in Fig. 13c. Abalos et al. (2012) have shown that for the  
 366 idealized case where upwelling dominates tracer transports, the ratio of tendencies for  
 367 two tracers ( $\chi_1, \chi_2$ ) is closely related to the ratio of the respective background gradients:

$$368 \quad \frac{\partial \bar{\chi}_1}{\partial t} / \frac{\partial \bar{\chi}_2}{\partial t} = \frac{\partial \bar{\chi}_1}{\partial z} / \frac{\partial \bar{\chi}_2}{\partial z} \sim \text{constant} \quad (2)$$

369 Integrating this equation in time for monthly O<sub>3</sub> and CO anomalies gives the relationship:

$$370 \quad \Delta \bar{O}_3 / \Delta \bar{CO} \approx \frac{\partial \bar{O}_3}{\partial z} / \frac{\partial \bar{CO}}{\partial z} \quad (3)$$

371 i.e. the ratio of monthly anomalies approximately follows the ratio of background vertical  
 372 gradients for the idealized situation where vertical transport is dominant. For the case of  
 373 CO and O<sub>3</sub> in the tropics near 68 hPa, the MERRA trajectory results yields a background

374 gradient ratio of  $\sim -18.34$  (ppbv km<sup>-1</sup>)/(ppmv km<sup>-1</sup>) for (dCO/dz) / (dO<sub>3</sub>/dz). A linear fit  
375 of the observed CO/O<sub>3</sub> anomalies (Fig. 13c) gives a ratio of  $-22.45 \pm 3.40$  (ppbv / ppmv),  
376 which is close to the idealized result (slightly outside of the two-sigma uncertainty). This  
377 approximate agreement with highly idealized theory provides further evidence for the  
378 control of tropical lower stratosphere O<sub>3</sub> and CO by variations in upwelling.

379

## 380 **5. Summary and Discussion**

381

382 The results presented here demonstrate that the domain-filling, forward trajectory  
383 model is useful for studying the transport of trace gases in the LS. The O<sub>3</sub> and CO  
384 simulations are complementary to modeling H<sub>2</sub>O (mainly controlled by tropopause  
385 temperature) in that O<sub>3</sub> and CO rely on both initial conditions and chemical production  
386 and loss rates, and are sensitive to transport. Initial conditions based on observations  
387 provide entry values of chemical species into the lower stratosphere; after that the  
388 chemical production and loss control the net changes of concentrations along the  
389 trajectories. Because the MERRA negative heating rates at 150-130 hPa (Fig. 1) prevent  
390 air ascending to the stratosphere, we chose a relatively high initialization level in the  
391 upper troposphere (370 K) in this study. However, we could have initiated parcels at  
392 lower altitude, such as 355 K when using ERAi circulation, to extend the results to the  
393 upper troposphere (UT).

394 Trajectory modeled O<sub>3</sub> and CO in the tropical lower stratosphere largely depend  
395 on the strength of upwelling (and to a lesser degree on the amount of mixing with  
396 extratropics, *Abalos et al.*, 2013a). Stronger upwelling is linked to faster transport, which  
397 results in less time for chemical production (for O<sub>3</sub>) or loss (for CO), leading to overall  
398 lower values of O<sub>3</sub> (Fig. 4a) and higher values of CO (Fig. 9a). The comparisons of  
399 MERRA and ERAi simulations that have different tropical upwelling rates (Q), e.g. Fig.  
400 1, clearly demonstrate this sensitivity. The detailed differences in diabatic heating rates  
401 among reanalyses have been discussed by Wright and Fueglistaler (2013), who highlight  
402 differences in the corresponding long-wave radiative heating rates in the lower  
403 stratosphere, which are influenced by both temperature and ozone. We also conducted a  
404 sensitivity study of increasing MERRA diabatic heating rates (Q) by constant factors, and

405 the best overall fit to the observations is 1.5 times the MERRA Q values, consistent with  
406 the ERAi-based results.

407 Although better agreement with observations of CO in the tropical lower  
408 stratosphere are found using ERAi data, there is reason to suspect that the ERAi diabatic  
409 heating in this region may be too high. For example, Ploeger et al. (2012) performed a  
410 radiative calculation showing that ERAi heating rates are ~40% too high, consistent with  
411 Schoeberl et al. (2012), who show that trajectory modeled water vapor tape recorder  
412 signal based on ERAi heating rates is ~30% too fast compared with MLS observations. In  
413 spite of the detailed differences, the trajectory modeled O<sub>3</sub> shows reasonable simulation  
414 of the large-scale seasonal structure compared to both MLS and WACCM, including both  
415 the tropics and the polar regions. The trajectory modeled CO in the tropical stratosphere  
416 is more sensitive to the MERRA vs. ERAi differences, likely because of the shorter  
417 photochemical lifetime of CO in the lower stratosphere compared to O<sub>3</sub>.

418 The annual cycles in O<sub>3</sub> and CO in the tropical LS are reproduced in the trajectory  
419 model simulations, and the magnitude of variations provides a useful test of the imposed  
420 circulation. The variability of O<sub>3</sub> and CO shows significant correlations with fluctuations  
421 in diabatic heating, for both seasonal and interannual time scales. These close  
422 relationships support the concept that tropical upwelling plays a key role in regulating  
423 variability for chemical species with strong vertical gradients in the lower stratosphere  
424 (and explains the observed compact relationships among interannual anomalies in  
425 diabatic heating, O<sub>3</sub> and CO seen in Figs. 12-13). For the idealized situation where  
426 upwelling dominates tracer transports, the tracer ratios can be expressed as ratios of the  
427 background vertical gradients, and the observed O<sub>3</sub> and CO changes are in approximate  
428 agreement with this expectation (Fig. 13c).

429 The discussion above linking seasonal or interannual changes in O<sub>3</sub> and CO with  
430 chemical changes along slower or faster upward trajectories is a Lagrangian perspective  
431 on transport (appropriate for our Lagrangian trajectory model). In contrast, the discussion  
432 linking O<sub>3</sub> and CO variations at particular pressure levels to varying circulations acting  
433 on background vertical gradients (Sect. 4) is an Eulerian perspective. These two  
434 perspectives are complementary and do not contradict each other; Abalos et al. (2013b)

435 have recently shown the equivalence of Lagrangian and Eulerian transport calculations in  
436 the tropical lower stratosphere, highlighting that each can provide useful information.

437 One limitation of this model is that it cannot account for interactions of  
438 circulation and chemistry, due to the climatological chemical production rates and loss  
439 frequencies adopted from WACCM (Section 2.2). This is most likely important in winter  
440 polar regions, where O<sub>3</sub> loss chemistry due to chlorine activation on polar stratospheric  
441 clouds is highly temperature dependent. Although we cannot simulate the detailed  
442 behavior in any particular (cold) year with climatological chemical ozone loss rates, our  
443 model does a reasonable job at simulating the time-average behavior of polar regions.

444 Our simulations with O<sub>3</sub> and CO have demonstrated the viability of the domain-  
445 filling forward trajectory model for simulating species with relatively simple chemistry,  
446 and extension to other species would be straightforward. There are several potential  
447 applications for such a trajectory model, including describing parcel histories that  
448 characterize different transport pathways, and evaluating the importance of tropical-  
449 extratropical exchanges. For example, trajectories can allow tracing the sources of CO-  
450 rich air in the summertime Asian monsoon region, and quantifying the fate of the parcels  
451 after breakup of the anticyclone. The model can also allow detailed comparisons of  
452 transport based on different and new reanalysis data sets, or idealized studies of the  
453 chemical responses to UTLS circulation in a changing climate.

454

455

456 *Acknowledgements.* We thank Kenneth Bowman, Laura Pan, Mijeong Park, Marta  
457 Abalos, Dominik Brunner, and Cameron Homeyer for their helpful discussions and  
458 comments. This work was supported by NSF AGS-1261948, NASA grant  
459 NNX13AK25G, and partially under the NASA Aura Science Program. This work has  
460 been partially carried out during visits of Tao Wang funded by the Graduate Student  
461 Visitor Program under the Advanced Study Program (ASP) at the National Center for  
462 Atmospheric Research (NCAR), which is operated by the University Corporation for  
463 Atmospheric Research, under sponsorship of the National Science Foundation.

464 **References**

- 465 Abalos, M., Randel, W. J., and Serrano, E.: Variability in upwelling across the tropical  
466 tropopause and correlations with tracers in the lower stratosphere, *Atmos. Chem.*  
467 *Phys.*, 12, 11505–11517, doi:10.5194/acp-12-11505-2012, 2012.
- 468 Abalos, M., Randel, W. J., Kinnison, D. E., and Serrano, E.: Quantifying tracer transport  
469 in the tropical lower stratosphere using WACCM, *Atmos. Chem. Phys.*, 13, 10591–  
470 10607, doi:10.5194/acp-13-10591-2013, 2013a.
- 471 Abalos, M., Ploeger, F., Konopka, P., Randel, W. J., and Serrano, E.: Ozone seasonality  
472 above the tropical tropopause: reconciling the Eulerian and Lagrangian perspectives of  
473 transport processes, *Atmos. Chem. Phys.*, 13, 10787–10794, doi:10.5194/acp-13-  
474 10787-2013, 2013b.
- 475 Andrews, D. G., Holton, J. R., and Leovy, C. B.: *Middle Atmosphere Dynamics*,  
476 Academic Press, Orlando, Florida, 489 pp., 1987.
- 477 Bernath, P. F., McElroy, C. T., Abrams, M. C., Boone, C. D., Butler, M., Camy-Peyret,  
478 C., Carleer, M., Clerbaux, C., Coheur, P. F., Colin, R., DeCola, P., Maziere, M. D.,  
479 Drummond, J. R., Dufour, D., Evans, W. F. J., Fast, H., Fussen, D., Gilbert, K.,  
480 Jennings, D. E., Llewellyn, E. J., Lowe, R. P., Mahieu, E., McConnell, J. C., McHugh,  
481 M., McLeod, S. D., Michaud, R., Midwinter, C., Nassar, R., Nichitu, F., Nowlan, C.,  
482 Rinsland, C. P., Rochon, Y. J., Rowlands, N., Semeniuk, K., Simon, P., Skelton, R.,  
483 Sloan, J. J., Soucy, M. A., Strong, K., Tremblay, P., Turnbull, D., Walker, K. A.,  
484 Walkty, I., Wardle, D. A., Wehrle, V., Zander, R., and Zou, J.: Atmospheric  
485 Chemistry Experiment (ACE): mission overview, *Geophys. Res. Lett.*, 32, L15S01,  
486 doi:10.1029/2005GL022386, 2005.
- 487 Bowman, K. P.: Large-scale isentropic mixing properties of the Antarctic polar vortex  
488 from analyzed winds, *J. Geophys. Res.*, 98, 23013–23027, 1993.
- 489 Bowman, K. P.: Transport of carbon monoxide from the tropics to the extratropics, *J.*  
490 *Geophys. Res.*, 111, D02107, doi:10.1029/2005JD006137, 2006.
- 491 Bowman, K. P. and Carrie, G. D.: The mean-meridional transport circulation of the  
492 troposphere in an idealized GCM, *J. Atmos. Sci.*, 59, 1502–1514, 2002.
- 493 Bowman, K. P., Lin, J. C., Stohl, A., Draxler, R., Konopka, P., Andrews, A., and  
494 Brunner, D.: Input data requirements Lagrangian Trajectory Models, *B. Am.*  
495 *Meteorol. Soc.*, 94, 1051–1058, doi:10.1175/BAMS-D-12-00076.1, 2013.
- 496 Clerbaux, C., George, M., Turquety, S., Walker, K. A., Barret, B., Bernath, P., Boone, C.,  
497 Borsdorff, T., Cammas, J. P., Catoire, V., Coffey, M., Coheur, P.-F., Deeter, M., De  
498 Mazière, M., Drummond, J., Duchatelet, P., Dupuy, E., de Zafra, R., Eddounia, F.,  
499 Edwards, D. P., Emmons, L., Funke, B., Gille, J., Griffith, D. W. T., Hannigan, J.,  
500 Hase, F., Höpfner, M., Jones, N., Kagawa, A., Kasai, Y., Kramer, I., Le Flochmoën,  
501 E., Livesey, N. J., López-Puertas, M., Luo, M., Mahieu, E., Murtagh, D., Nédélec, P.,  
502 Pazmino, A., Pumphrey, H., Ricaud, P., Rinsland, C. P., Robert, C., Schneider, M.,  
503 Senten, C., Stiller, G., Strandberg, A., Strong, K., Sussmann, R., Thouret, V.,  
504 Urban, J., and Wiacek, A.: CO measurements from the ACE-FTS satellite instrument:  
505 data analysis and validation using ground-based, airborne and spaceborne  
506 observations, *Atmos. Chem. Phys.*, 8, 2569–2594, doi:10.5194/acp-8-2569-2008,  
507 2008.
- 508 Crutzen, P. J.: A discussion of the chemistry of some minor constituents in the

509 stratosphere and troposphere, *Pure Appl. Geophys.*, 106, 1385–1399, 1973.

510 Dee, D. P., Uppala, S. M., Simmons, A. J., Berrisford, P., Poli, P., Kobayashi, S., Andrae,  
511 U., Balmaseda, M. A., Balsamo, G., Bauer, P., Bechtold, P., Beljaars, A. C. M., van de  
512 Berg, 5 L., Bidlot, J., Bormann, N., Delsol, C., Dragani, R., Fuentes, M., Geer, A. J.,  
513 Haimberger, L., Healy, S. B., Hersbach, H., Hólm, E. V., Isaksen, I., Kållberg, P.,  
514 Köhler, M., Matricardi, M., McNally, A. P., Monge-Sanz, B. M., Morcrette, J.-J.,  
515 Park, B.-K., Peubey, C., de Rosnay, P., Tavolato, C., Thépaut, J.-N., and Vitart, F.:  
516 The ERA-Interim reanalysis: configuration and performance of the data assimilation  
517 system, *Q. J. Roy. Meteor. Soc.*, 137, 553–597, doi:10.1002/qj.828, 2011.

518 Dessler, A. E.: A reexamination of the “stratospheric fountain” hypothesis, *Geophys.*  
519 *Res. Lett.*, 25, 4165–4168, doi:10.1029/1998GL900120, 1998.

520 Dessler, A. E.: *The Chemistry and Physics of Stratospheric Ozone*, International  
521 *Geophysics Series*, Vol. 74, Academic Press, San Diego, 221 pp., 2000.

522 Dessler, A. E., Schoeberl, M. R., Wang, T., Davis, S. M., and Rosenlof, K. H.  
523 Stratospheric water vapor feedback, *P. Natl. Acad. Sci. USA*, 110, 18087–18091,  
524 doi:10.1073/pnas.1310344110, 2013.

525 Fischer, H., Wienhold, F. G., Hoor, P., Bujok, O., Schiller, C., Siegmund, P., Ambaum,  
526 M., Scheeren, H. A., and Lelieveld, J.: Tracer correlations in the northern high latitude  
527 lower- 20 most stratosphere: influence of cross-tropopause mass exchange, *Geophys.*  
528 *Res. Lett.*, 27, 97–100, doi:10.1029/1999GL010879, 2000.

529 Folkins, I., Braun, C., Thompson, A. M., and Witte, J.: Tropical ozone as an indicator of  
530 deep convection, *J. Geophys. Res.*, 107, D13, doi:10.1029/2001JD001178, 2002.

531 Froidevaux, L., Jiang, Y. B., Lambert, A., Livesey, N. J., Read, W. G., Waters, J. W.,  
532 Browell, E. V., Hair, J. W., Avery, M. A., Mcgee, T. J., Twigg, L. W., Sunmicht, G.  
533 K., Jucks, K. W., Margitan, J. J., Sen, B., Stachnik, R. A., Toon, G. C., Bernath, P. F.,  
534 Boone, C. D., Walker, K. A., Filipiak, M. J., Harwood, R. S., Fuller, R. A., Manney,  
535 G. L., Schwartz, M. J., Daffer, W. H., Drouin, B. J., Cofield, R. E., Cuddy, D. T.,  
536 Jarnot, R. F., Knosp, B. W., Perun, V. S., Snyder, W. V., Stek, P. C., Thurstans, R. P.,  
537 and Wagner, P. A.: Validation of Aura Microwave Limb Sounder stratospheric ozone  
538 measurements, *J. Geophys. Res.*, 113, D15S20, doi:10.1029/2007JD008771, 2008.

539 Fueglistaler, S., Bonazzola, M., Haynes, P. H., and Peter, T.: Stratospheric water vapor  
540 predicted from the Lagrangian temperature history of air entering the stratosphere in  
541 the tropics, *J. Geophys. Res.*, 110, D08107, doi:10.1029/2004JD005516, 2005.

542 Fueglistaler, S., Dessler, A. E., Dunkerton, T. J., Folkins, I., Fu, Q., and Mote, P. W.: The  
543 tropical tropopause layer, *Rev. Geophys.*, 47, RG1004, doi:10.1029/2008RG000267,  
544 2009.

545 Garcia, R. R., Marsh, D. R., Kinnison, D. E., Boville, B. A., and Sassi, F.: Simulation of  
546 secular trends in the middle atmosphere, 1950–2003, *J. Geophys. Res.*, 112, D09301,  
547 doi:10.1029/2006JD007485, 2007.

548 Jiang, J. H., Livesey, N. J., Su, H., Neary, L., McConnell, J. C., and Richards, N. A. D.:  
549 Connect- ing surface emissions, convective uplifting, and long-range transport of  
550 carbon monoxide in the upper troposphere: new observations from the Aura  
551 Microwave Limb Sounder, *Geophys. Res. Lett.*, 34, L18812,  
552 doi:10.1029/2007GL030638, 2007.

553 Lamarque, J.-F., Emmons, L. K., Hess, P. G., Kinnison, D. E., Tilmes, S., Vitt, F., Heald,  
554 C. L., Holland, E. A., Lauritzen, P. H., Neu, J., Orlando, J. J., Rasch, P. J., and

555 Tyndall, G. K.: CAM-chem: description and evaluation of interactive atmospheric  
556 chemistry in the Community Earth System Model, *Geosci. Model Dev.*, 5, 369–411,  
557 doi:10.5194/gmd-5-369-2012, 2012.

558 Liu, C., Zipser, E., Garrett, T., Jiang, J. H., and Su, H.: How do the water vapor and  
559 carbon monoxide “tape recorders” start near the tropical tropopause?, *Geophys. Res.*  
560 *Lett.*, 34, L09804, doi:10.1029/2006GL029234, 2007.

561 Liu, Y. S., Fueglistaler, S., and Haynes, P. H.: Advection-condensation paradigm for  
562 strato- spheric water vapor, *J. Geophys. Res.*, 115, D24307,  
563 doi:10.1029/2010jd014352, 2010.

564 Livesey, N. J., Filipiak, M., Froidevaux, L., Read, W. G., Lambert, A., Santee, M. L.,  
565 Jiang, J. H., Pumphrey, Hugh, Waters, J. W., Cofield, R. E., Cuddy, D. T., Daffer, W.  
566 H., Drouin, B. J., Fuller, R. A., Jarnot, R. F., Jiang, Y. B., Knosp, B. W., Li, Q. B.,  
567 Perun, V. S., Schwartz, M. J., Snyder, W. V., Stek, P. C., Thurstans, R. P., Wagner, P.  
568 A., Avery, M., Browell, E. V., Cammas, J. -P., Christensen, L. E., Diskin, G. S., Gao,  
569 R.-S., Jost, H.-J., Loewenstein, M., Lopez, J. D., Nedelec, P., Osterman, G. B.,  
570 Sachse, G. W., and Webster, C. R.: Validation of Aura Microwave Limb Sounder O<sub>3</sub>  
571 and CO observations in the upper troposphere and lower stratosphere, *J. Geophys.*  
572 *Res.*, 113, D15S02, doi:10.1029/2007JD008805, 2008.

573 Logan, J., Prather, M., Wofsy, S., and McElroy, M.: Tropospheric chemistry: a global  
574 perspec- tive, *J. Geophys. Res.*, 86, 7210–7254, doi:10.1029/JC086iC08p07210, 1981.

575 Mote, P. W., Rosenlof, K. H., McIntyre, M. E., Carr, E. S., Gille, J. C., Holton, J. R.,  
576 Kinnersley, J. S., Pumphrey, H. C., Russell III, J. M., and Waters, J. W.: An  
577 atmospheric tape recorder: the imprint of tropical tropopause temperatures on  
578 stratospheric water vapor, *J. Geophys. Res.*, 101, 3989–4006, 1996.

579 Park, M., Randel, W. J., Emmons, L. K., and Livesey, N. J.: Transport pathways of  
580 carbon monoxide in the Asian summer monsoon diagnosed from Model of Ozone and  
581 Related Tracers (MOZART), *J. Geophys. Res.*, 114, D08303,  
582 doi:10.1029/2008JD010621, 2009.

583 Park, M., Randel, W. J., Kinnison, D. E., Emmons, L. K., Bernath, P. F., Walker, K. A.,  
584 Boone, C. D., and Livesey, N. J.: Hydrocarbons in the upper troposphere and lower  
585 strato- sphere observed from ACE-FTS and comparisons with WACCM, *J. Geophys.*  
586 *Res.-Atmos.*, 118, 1964–1980, doi:10.1029/2012JD018327, 2013.

587 Ploeger, F., Konopka, P., Gunther, G., Grooss, J. U., and Muller, R.: Impact of the  
588 vertical velocity scheme on modeling transport in the tropical tropopause layer, *J.*  
589 *Geophys. Res.*, 115, D03301, doi:10.1029/2009jd012023, 2010.

590 Ploeger, F., Konopka, P., Müller, R., Fueglistaler, S., Schmidt, T., Manners, J. C., Grooß,  
591 J.-U., Günther, G., Forster, P. M., and Riese, M.: Horizontal transport affecting trace  
592 gas seasonality in the Tropical Tropopause Layer (TTL), *J. Geophys. Res.*, 117,  
593 D09303, doi:10.1029/2011JD017267, 2012.

594 Pumphrey, H. C., Filipiak, M. J., Livesey, N. J., Schwartz, M. J., Boone, C., Walker, K.  
595 A., Bernath, P., Ricaud, P., Barret, B., Clerbaux, C., Jarnot, R. F., Manney, G. L., and  
596 Waters, J. W.: Validation of middle-atmosphere carbon monoxide retrievals from the  
597 Microwave Limb Sounder on Aura, *J. Geophys. Res.*, 112, D24S38,  
598 doi:10.1029/2007JD008723, 2007.

599 Randel, W. J. and Jensen, E. J.: Physical processes in the tropical tropopause layer and  
600 their role in a changing climate, *Nat. Geosci.*, 6, 169–176, doi:10.1038/ngeo1733,

601 2013.

602 Randel, W. J. and Park, M.: Deep convective influence on the Asian summer monsoon  
603 an- ticyclone and associated tracer variability observed with Atmospheric Infrared  
604 Sounder (AIRS), *J. Geophys. Res.*, 111, D12314, doi:10.1029/2005JD006490, 2006.

605 Randel, W., Park, M., Wu, F., and Livesey, N.: A large annual cycle in ozone above the  
606 tropical tropopause linked to the Brewer–Dobson Circulation, *J. Atmos. Sci.*, 64,  
607 4479–4488, 2007.

608 Randel, W. J., Park, M., Emmons, L., Kinnison, D., Bernath, P., Walker, K., Boone, C.,  
609 and Pumphrey, H.: Asian monsoon transport of pollution to the stratosphere, *Science*,  
610 328, 611– 613, doi:10.1126/science.1182274, 2010.

611 Rienecker, M. M., Suarez, M. J., Gelaro, R., Todling, R., Bacmeister, J., Liu, E.,  
612 Bosilovich, M. G., Schubert, S.D., Takacs, L., Kim, G.-K., Bloom, S., Chen, J.,  
613 Collins, D., Conaty, A., da Silva, A., Gu, W., Joiner, J., Koster, R. D., Lucchesi, R.,  
614 Molod, A., Owens, T., Pawson, S., Pegion, P., Redder, C. R., Reichle, R., Robertson,  
615 F. R., Ruddick, A. G., Sienkiewicz, M., and Woollen, J.: MERRA – NASA’s modern-  
616 era retrospective analysis for research and applications, *J. Climate*, 24, 3624–3648,  
617 doi:10.1175/JCLI-D-11-00015.1, 2011.

618 Schoeberl, M. R. and Dessler, A. E.: Dehydration of the stratosphere, *Atmos. Chem.*  
619 *Phys.*, 11, 8433–8446, doi:10.5194/acp-11-8433-2011, 2011.

620 Schoeberl, M. R., Douglass, A. R., Zhu, Z., and Pawson, S.: A comparison of the lower  
621 strato- spheric age spectra derived from a general circulation model and two data  
622 assimilation sys- tems, *J. Geophys. Res.*, 108, 4113, doi:10.1029/2002JD002652,  
623 2003.

624 Schoeberl, M. R., Duncan, B. N., Douglass, A. R., Waters, J., Livesey, N., Read, W., and  
625 Filipiak, M.: The carbon monoxide tape recorder, *Geophys. Res. Lett.*, 33, L12811,  
626 doi:10.1029/2006GL026178, 2006.

627 Schoeberl, M. R., Douglass, A. R., Newman, P. A., Lait, L. R., Lary, D., Waters, J.,  
628 Livesey, N., Froidevaux, L., Lambert, A., Read, W., Filipiak, M. J., and Pumphrey,  
629 H.C.: QBO and annual cycle variations in tropical lower stratosphere trace gases from  
630 HALOE and Aura MLS observations, *J. Geophys. Res.*, 113, D05301,  
631 doi:10.1029/2007JD008678, 2008.

632 Schoeberl, M. R., Dessler, A. E., and Wang, T.: Simulation of stratospheric water vapor  
633 and trends using three reanalyses, *Atmos. Chem. Phys.*, 12, 6475–6487,  
634 doi:10.5194/acp-12- 6475-2012, 2012.

635 Schoeberl, M. R., Dessler, A. E., and Wang, T.: Modeling upper tropospheric and lower  
636 strato- spheric water vapor anomalies, *Atmos. Chem. Phys.*, 13, 7783–7793,  
637 doi:10.5194/acp-13- 7783-2013, 2013.

638 Wang, T. and Dessler, A. E.: Analysis of cirrus in the tropical tropopause layer from  
639 CALIPSO and MLS data: a water perspective, *J. Geophys. Res.*, 117, D04211,  
640 doi:10.1029/2011JD016442, 2012.

641 Waters, J. W., Froidevaux, L., Harwood, R. S., Jarnot, R. F., Pickett, H. M., Read, W. G.,  
642 Siegel, P. H., Cofield, R. E., Filipiak, M. J., Flower, D. A., Holden, J. R., Lau, G. K.,  
643 K., Livesey, N. J., Manney, G. L., Pumphrey, H. C., Santee, M. L., Wu, D. L., Cuddy,  
644 D. T., Lay, R. R., Loo, M. S., Perun, V. S., Schwartz, M. J., Stek, P. C., Thurstans, R.  
645 P., Boyles, M. A., Chandra, K. M., Chavez, M. C., Chen, G. S., Chudasama, B. V.,  
646 Dodge, R., Fuller, R. A., Girard, M. A., Jiang, J. H., Jiang, Y. B., Knosp, B. W.,

647 LaBelle, R. C., Lam, J. C., Lee, K. A., Miller, D., Oswald, J. E., Patel, N. C., Pukala,  
648 D. M., Quintero, O., Scaff, D. M., Van Snyder, W., Tope, M. C., Wagner, P. A., and  
649 Walch, M. J.: The Earth Observing System Microwave Limb Sounder (EOS MLS) on  
650 the Aura satellite, *IEEE T. Geosci. Remote*, 44, 1075–1092, 2006.  
651 Waugh, D. W., Hall, T. M., Age of stratospheric air: theory, observations, and models,  
652 *Rev. Geophys.*, 40, 1010, doi:10.1029/2000RG000101, 2002.  
653 Winker, D. and Trepte, C.: Laminar cirrus observed near the tropical tropopause by  
654 LITE, *Geophys. Res. Lett.*, 25, 3351–3354, 1998.  
655 Wright, J. S. and Fueglistaler, S.: Large differences in reanalyses of diabatic heating in  
656 the tropical upper troposphere and lower stratosphere, *Atmos. Chem. Phys.*, 13, 9565–  
657 9576, doi:10.5194/acp-13-9565-2013, 2013.  
658

659 **Figures**  
660  
661  
662

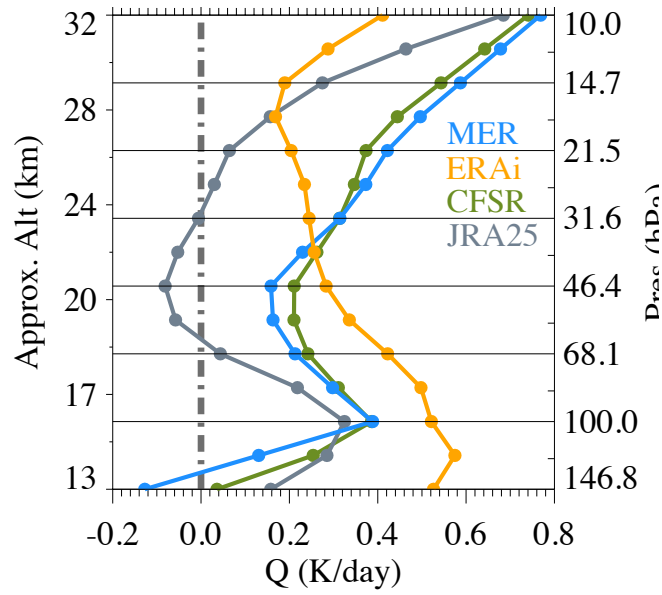


**Fig. 1.** Comparison of total diabatic heating rates averaged over the deep tropics (18° N-S) in 2000-2010 from four different reanalysis data sets: MER (MERRA), ERAi (ECMWF ERA interim), CFSR (NCEP CFSR) and JRA25.

663

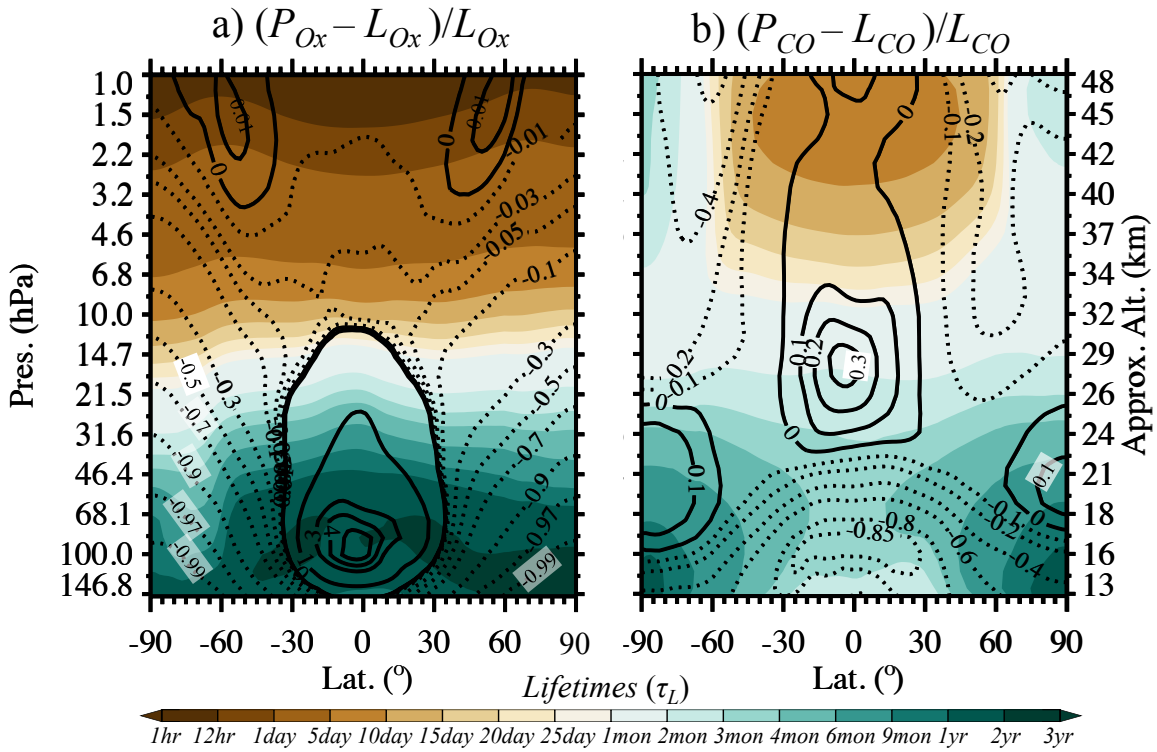


**Fig. 2.** The ratio of chemical net tendency (production rate minus loss rate) to loss rate from WACCM for (a)  $O_x$  and (b) CO. Negative numbers are dashed to highlight the net chemical decrease and positive numbers indicate net chemical increase, while zero lines indicate comparable amount of production and loss. For reference, the respective  $O_x$  and CO lifetimes are contoured in color.

664  
 665  
 666  
 667

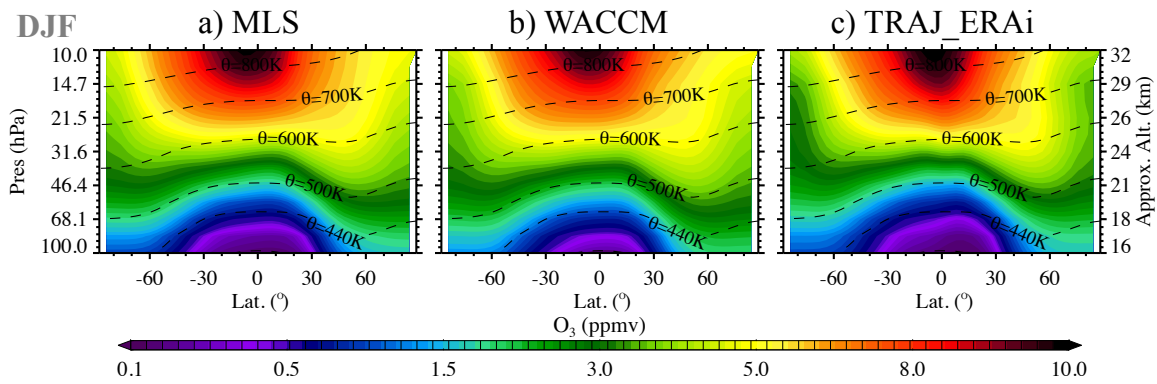


**Fig. 3.** Trajectory modeled O<sub>3</sub> driven by ERAi reanalysis wind (**c**, TRAJ\_ERAI) in boreal winter (DJF), compared to both MLS observations (**a**) and WACCM output (**b**). Both WACCM and trajectory model results are weighted by the MLS averaging kernels. Dashed lines are potential temperature contours, demonstrating that in the lower LS where transport dominates, chemical distributions roughly follow the isentropes.

668  
669

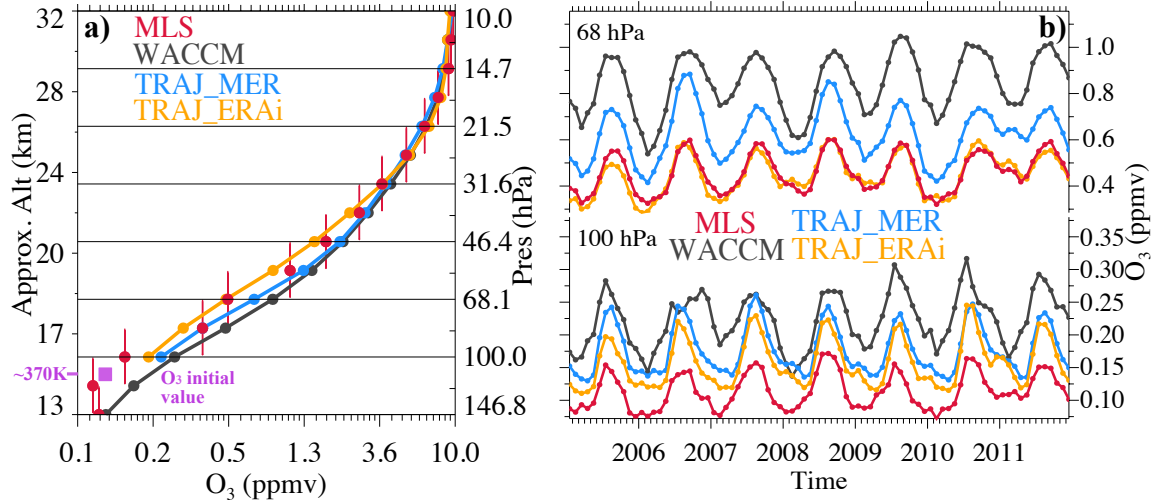


**Fig. 4.** Tropical (a) vertical profile and (b) time series (100 hPa, bottom panel; 68 hPa, upper panel) of MLS, WACCM, and trajectory modeled O<sub>3</sub> driven by MERRA wind and ERAi wind, averaged over the deep tropics (18° N-S) from 2005 to 2011. Both WACCM and trajectory model results are weighted by the MLS averaging kernels. In (a) the x-axis is in log scale to highlight the differences; the purple square indicates the initial O<sub>3</sub> values carried by parcels when they were first injected into the domain at 370 K; the vertical bars in red indicate the MLS vertical resolutions at each of the MLS retrieval pressure levels.

670

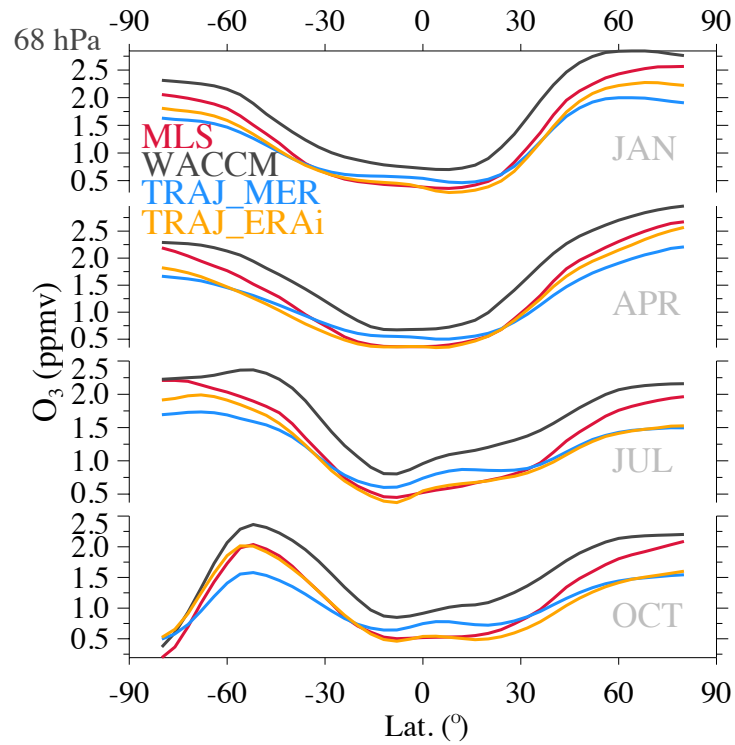


**Fig. 5.** Zonal mean of  $O_3$  at 68-hPa during January (JAN), April (APR), July (JUL), and October (OCT) averaged in 2005-2011 from MLS, WACCM, and trajectory results driven by MERRA wind and ERAi wind. Both WACCM and trajectory model results are weighted by the MLS averaging kernels. In October (Antarctic spring time), the South Pole undergoes exceptional depletion of  $O_3$ .

671

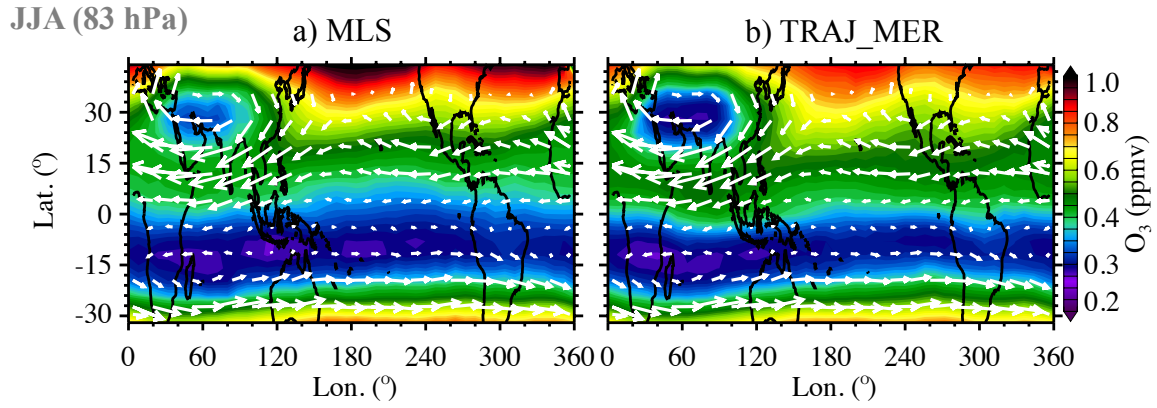


**Fig. 6.** Northern Hemisphere Summertime (JJA) tropical O<sub>3</sub> distributions at 83 hPa averaged from 2005 to 2011 between MLS and the MERRA driven trajectory simulations (weighted by the MLS averaging kernels). Horizontal wind vectors from the MERRA reanalysis are overlaid to emphasize the Asian summer monsoon anticyclone.

672

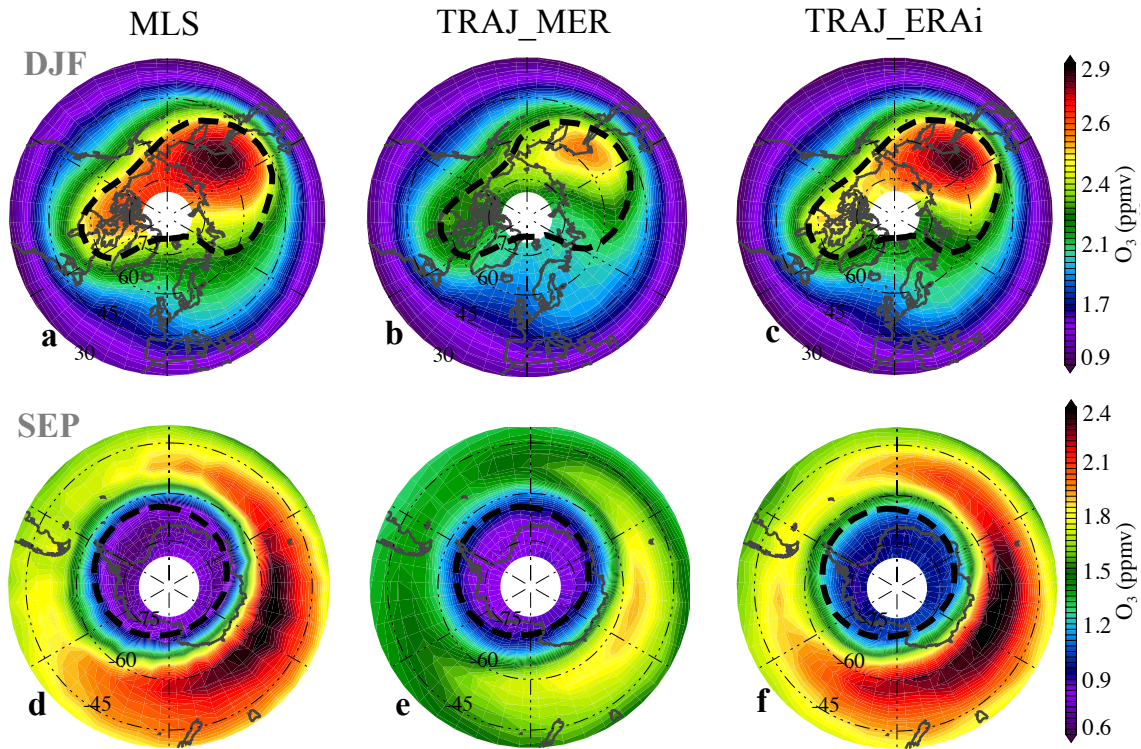


**Fig. 7.** Polar O<sub>3</sub> distributions shown in MLS (left column), trajectory results driven by MERRA (middle column), and trajectory results driven by ERAi (right column) during Northern Hemisphere winter (DJF, **a-c**) and Southern Hemisphere spring (September, SEP, **d-f**) at 68 hPa. Trajectory results are weighted by the MLS averaging kernels. The 24-PVU potential vortices (**a-c**) and the 195-K temperature (**d-f**) are overlaid in black dashed lines for both seasons, respectively.

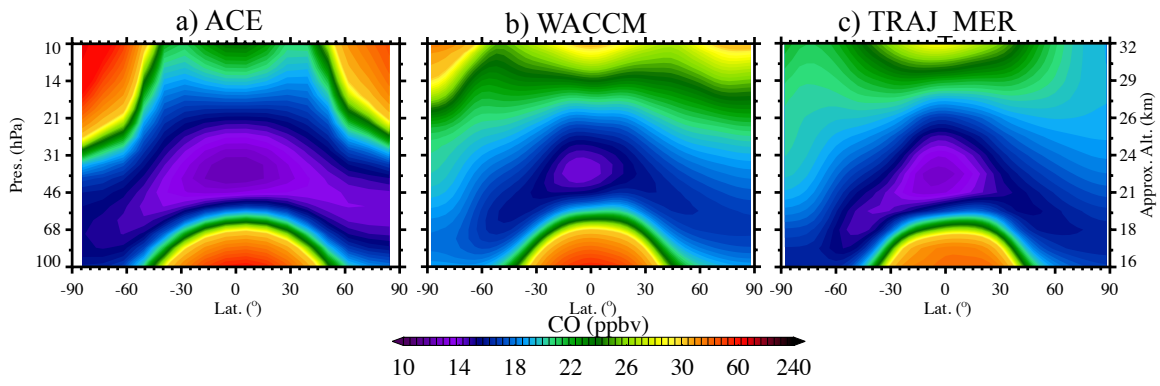


**Fig. 8.** Zonal mean cross sections of CO from (a) ACE-FTS, (b) WACCM, and (c) trajectory model driven by MERRA reanalysis.

674

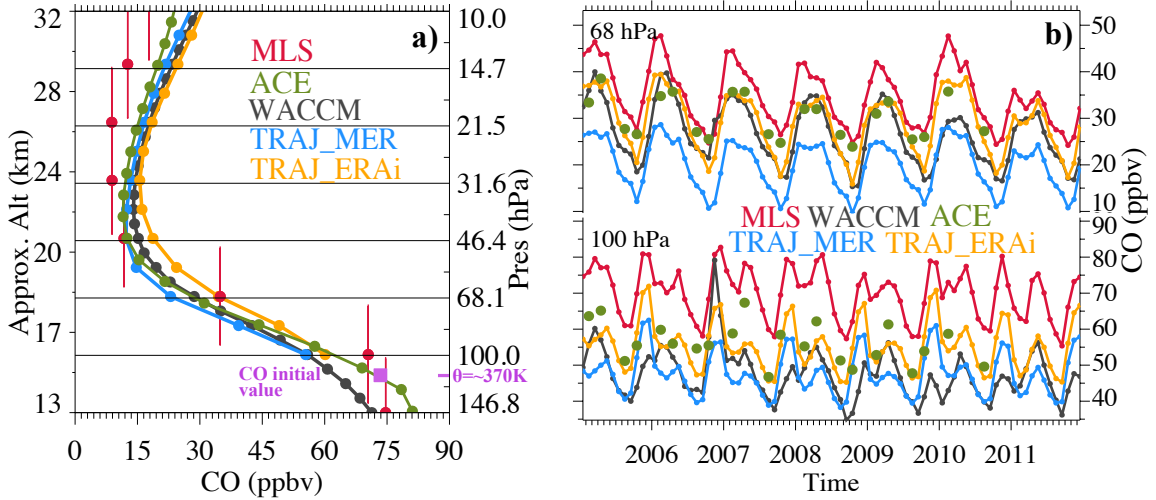


**Fig. 9.** Tropical (a) vertical profile and (b) time series (100 hPa, bottom panel; 68 hPa, upper panel) of MLS, WACCM, ACE, and trajectory modeled CO driven by MERRA wind and ERAI wind, averaged over 15° N-S from 2005 to 2011. In (b) the WACCM and trajectory model results are weighted by the MLS averaging kernels. In (a) the purple square indicates the initial CO values carried by parcels when they were first injected into the domain at 370 K, and vertical bars in red indicate the MLS vertical resolutions at each of the MLS retrieval pressure levels.

675  
676

677  
678

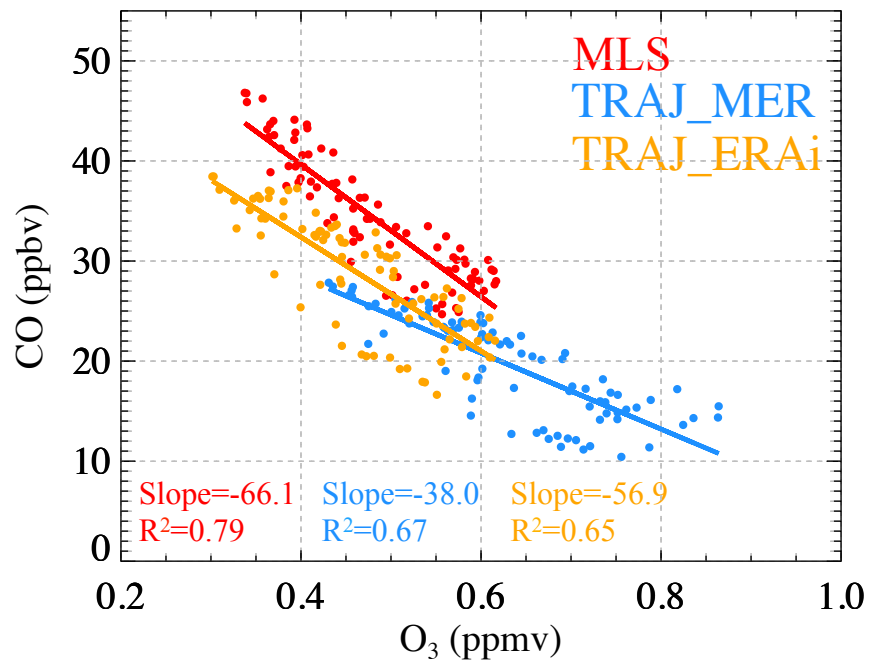


**Fig. 10.** Monthly variations of O<sub>3</sub> vs. CO in the tropical lower stratosphere (15° N-S, 68 hPa) from MLS and trajectory modeling driven by MERRA wind and ERAi wind. Trajectory results are weighted by the MLS averaging kernels.

679

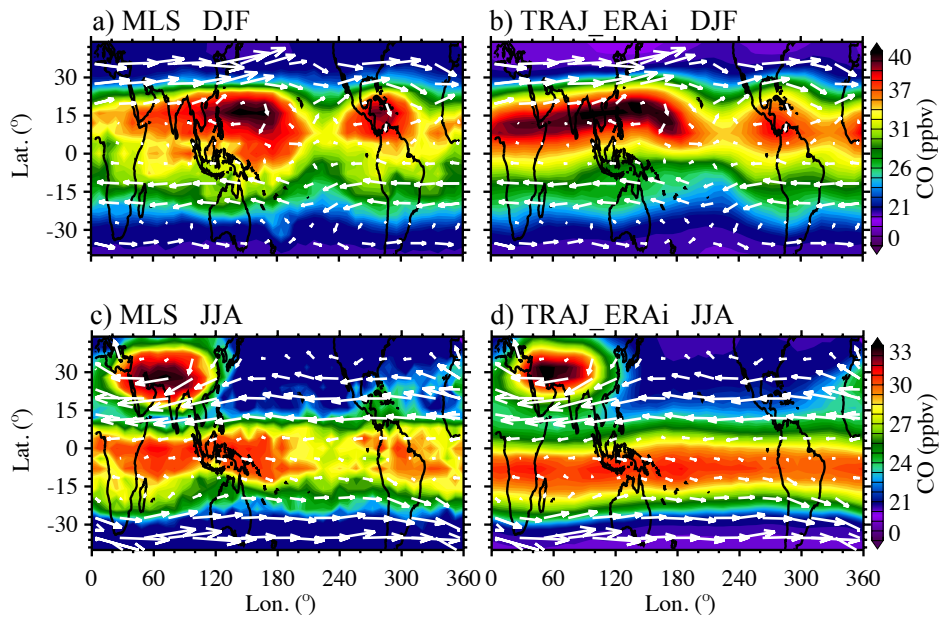


**Fig. 11.** Comparison of CO at 68 hPa ( $\sim 20$  km) during DJF (top row, **a** and **b**) and JJA (bottom row, **c** and **d**) between MLS (left) and trajectory modeling driven by ERAi wind (right, weighted by the MLS averaging kernels). Horizontal wind vectors from ERAi are overlaid as reference.

680

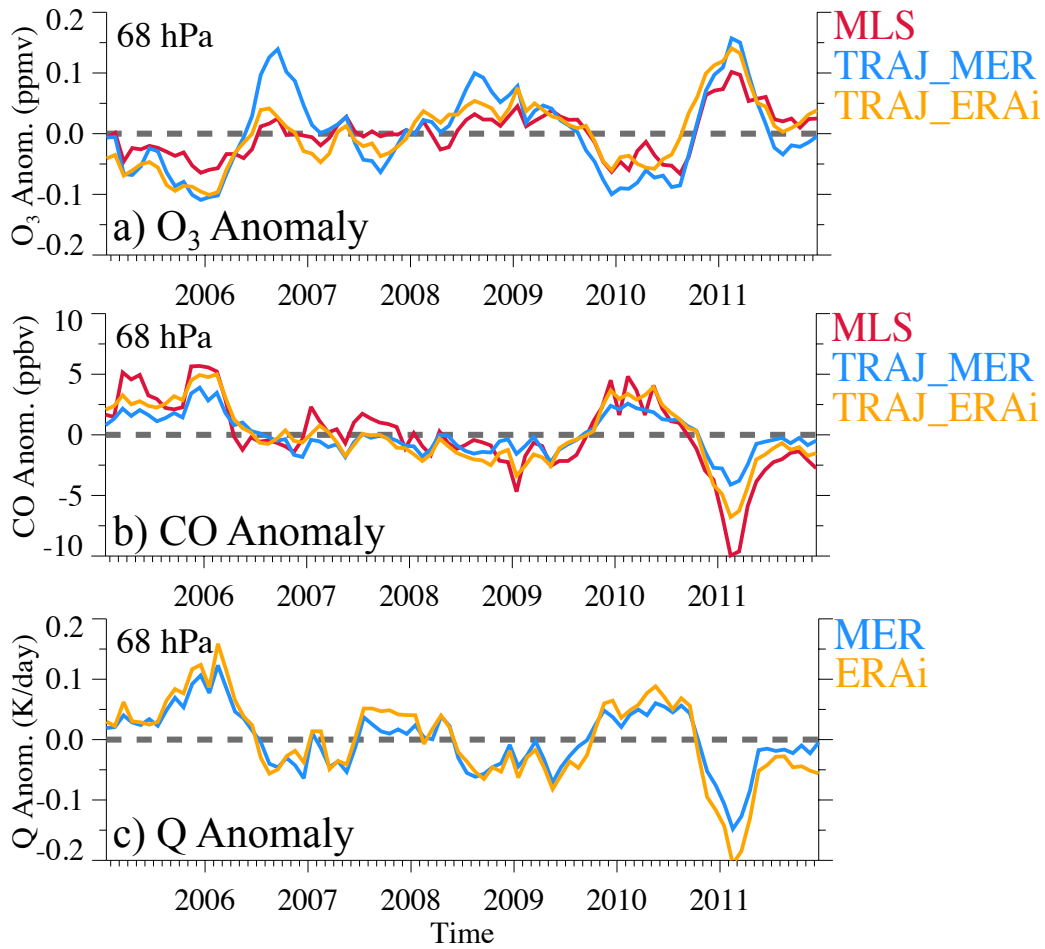


**Fig. 12.** Interannual anomalies of (a) O<sub>3</sub> and (b) CO from MLS (red) and trajectory simulations driven by MERRA and ERAi in the tropical (15° N-S) lower stratosphere (68 hPa). (c) shows interannual anomalies of total diabatic heating rates from MERRA and ERAi, which serves in our model as the vertical velocity. The trajectory results are weighted by the MLS averaging kernels.

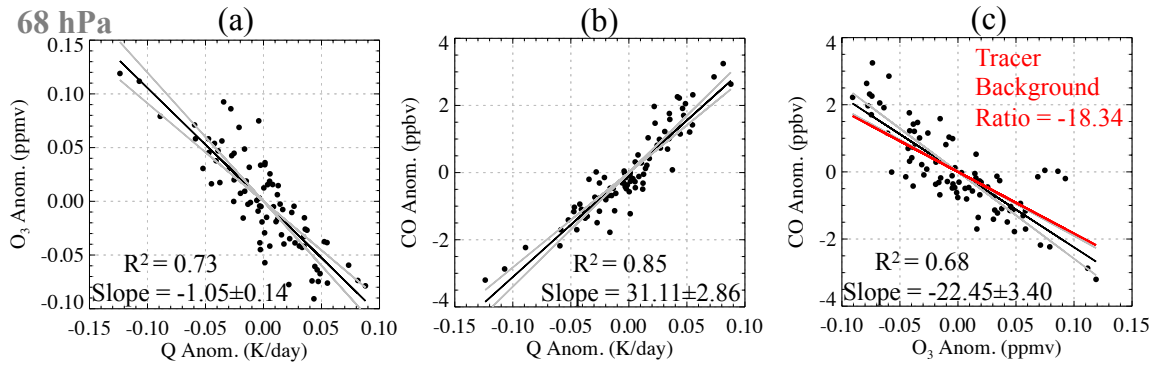


**Figure 13.** Scatter plots of the anomalies of (a) O<sub>3</sub> vs. Q and (b) CO vs. Q, and (c) CO vs. O<sub>3</sub> at 68 hPa. The dots are monthly variations of tracers from trajectory modeling driven by MERRA winds and diabatic heating rates; the black lines show the linear fit. The red line in (c) is the theoretically estimated tracer ratio estimated from the respective background gradients, using simplified relation in Eq. (3).

682